Underwater Time of Flight Camera Rangefinding with Backscatter Phasor Subtraction

Austin Jantzi, William Jemison, Prashant Athavale, Mahesh Banavar, and Erik Bollt
Dept. of Electrical and Computer Engineering
Clarkson University
Potsdam, New York 13699
Email: jantziaw@clarkson.edu

Luke Rumbaugh
Dept. of Electrical and Computer Engineering
Grove City College
Grove City, PA 16127

David Illig
Warfighter Basic and Applied Research Division
NAWCAD
Patuxent River, Maryland 20670

***Abstract*—Time-of-flight (ToF) cameras are a recently developed tool for measuring and mapping 3D space. These cameras have potential for underwater applications, however their performance is limited by scattering in many underwater environments. This work uses a phasor subtraction method to overcome some of the limits imposed on ToF cameras due to scattering. Experimental results demonstrate the efficacy of this method, doubling the operating range of the raw camera performance.**

I. Introduction

Light detection and ranging (Lidar) is a method used to obtain high resolution depth and spatial information in challenging, underwater environments [1]–[4]. The performance of underwater lidar systems is limited by two fundamental interactions between light and turbid (*i.e.* murky) water: absorption and scattering. Both water and the particulates suspended in water absorb light, removing optical intensity from the scene and limiting the maximum operating range of lidar systems[5]. In this work, we address absorption by using green light, which minimizes absorption in turbid water[6]. However, many cases of interest, such as harbors, bays, and coastlines are limited by scattering rather than absorption. Light that reflects off of the suspended particulates and returns to the detector without interacting with any submerged object is referred to as backscatter. Backscatter limits the performance of lidar systems by reducing image contrast and reducing the signal-to-noise ratio (SNR). Light which reflects off of an object but still scatters at small angles before detection is referred to as forward scatter. Forward scattered light takes a slightly longer path than light which returns directly from an object which leads to range error (due to the delayed time of arrival) and pixel to pixel blurring in images.

Scattering limited environments are more challenging than absorption limited environments, and a number of approaches have been developed to address these environments[7]. Range gating only opens the detector after a time delay to reduce the collection of backscatter[8], [9]. Hybrid lidar-radar modulates the lidar beam intensity with a radar sub-carrier[10]. A number of techniques hardware and software techniques have been developed for hybrid lidar-radar to mitigate the effects of scattering in turbid underwater environments[11]–[18]. Simultaneous scanning of a laser and a narrow field of view (FOV) receiver is another technique to reduce the collection of scattered light. This method minimizes the common volume overlap between the transmitter and the receiver.[4]. More recent techniques have focused on the use of specialized optical elements to perform wavefront coding to reduce the impact of scattering on communications as well as rangefinding[19]–[35].

ToF cameras are tools which are increasingly used for 3D mapping and modeling in underwater environments[36]–[38]. ToF cameras generate phase (which can be translated to range using the modulation frequency) and amplitude images of a scene at video rates with centimeter scale depth resolution[39]. However, like all underwater lidar systems, the performance of these systems are limited by multipath interference[40], caused by backscattering from the turbid water. In this paper we describe a method and show experimental results to mitigate the effect of backscattering on ToF camera phase and range measurements, improving the accuracy and extending the operating range of the ToF camera. We explain the details of the method in Section II and Section III and experimental results are shown in IV.

II. Background

A. ToF Phase and Amplitude Measurements in Turbid Water

We use the ToF camera to simultaneously images the phase and amplitude of a scene. This is done by modulating the transmit beams and demodulating the return phase in-quadrature at each pixel. We quantify the performance of the ToF camera in terms of attenuation lengths, cz, where c is the extinction coefficient of the turbid water water and z is the range to the submerged object. Greater attenuation lengths have greater degrees of scattering and absorption, which limits the performance of the ToF camera. Greater absorption decreases the signal from the object. Scattering generates clutter which interferes with the collection of light from the object. Instead of just the optical return from a submerged object, the camera sees two returns: one from the submerged object and another from the backscattered light. Due to the ToF camera's processing, the total return is the

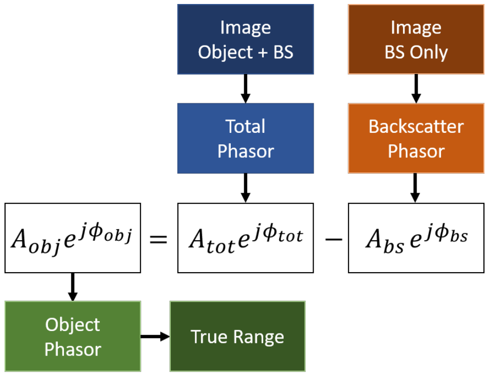

Fig. 1. Backscatter phasor subtraction method. The ToF camera calibrates by imaging the backscatter only (*i.e.* the light returning from the underwater environment). Images collected during the normal operation of the ToF camera are a phasor sum of the light reflected from any submerged objects and the backscattered light. The backscatter only phasor is subtracted from the object+backscatter phasor, resulting in the amplitude, phase, and true range of the underwater object.

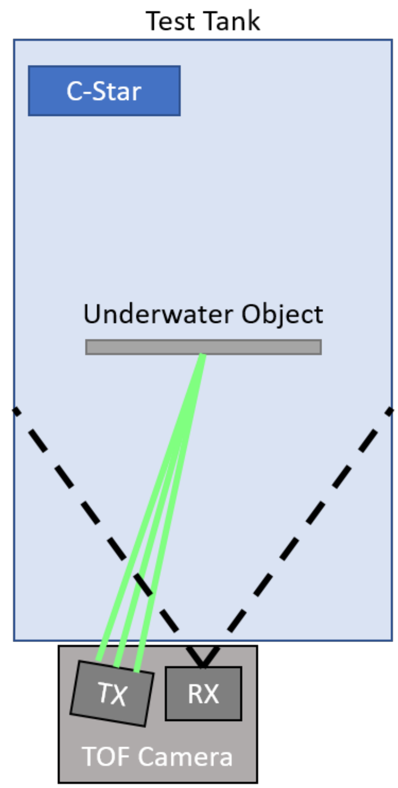

Fig. 2. The experimental setup for the ToF camera measurements. For each measurement, a C-Star transmissometer measures the turbidity. When imaging total amplitude and total phase a flat, gray, spray painted PVC objected is submerged in the lidar test tank. Three laser diodes transmit light into the test tank. The ToF camera images the scene (the FOV is shown as dashed, black lines).

sum of these contributions[40]. We define this relationship as the sum of two phasors:

$$A_{tot}e^{j\phi_{tot}} = A_{obj}e^{j\phi_{obj}} + A_{bs}e^{j\phi_{bs}}, \tag{1}$$

where A_{tot} is the total amplitude measured by the camera, A_{obj} is the amplitude from the object, A_{bs} is the amplitude of the backscatter, and ϕ is the respective phase value measured by the camera, of the object, and of the backscatter[41]. This model accounts for the object and backscatter, but in its present form assumes there is no contribution from forward scattering. This leads to some additional range error (seen in Section IV). However, the contribution of backscatter is much larger than that of forward scatter, meaning that this simple model is still able to improve the accuracy of the ToF system. Figure 1 summarizes the method for backscatter phasor subtraction. Experimentally, the raw ToF camera images both the object and the backscatter, generating the total phasor. To image only the backscatter, we remove the underwater object from the test tank and generate the backscatter phasor with thee ToF camera. Rearranging Eq. 1 and using the measured phasors,

$$A_{obj}e^{j\phi_{obj}} = A_{tot}e^{j\phi_{tot}} - A_{bs}e^{j\phi_{bs}}, \tag{2}$$

we calculate the object phasor. The true range to the object is then calculated from object phasor and the modulation frequency of the ToF camera.

III. Methods

A. Experimental Setup

We show the experimental setup in Fig. 2. The ToF camera is based on a modified Espros EPC660 evaluation kit[37]. The infrared diodes are replaced by three, 1 W, 532 nm laser diodes modulated at 24 MHz. For the ToF camera, there are inherent trade-offs between the maximum operating range and the beam spread (which determines how much of the scene is filled with light). The maximum operating range is achieved by maximizing the power density (*i.e.* transmitting collimated beams). However, transmitting collimated beams instead of diverging beams (which have a lower power density) fills less of the scene with light. In this work, we seek to maximize the operating range of the ToF camera and transmit collimated beams. Future work will explore higher power transmitters as well as diverging beams at shorter attenuation lengths.

The ToF camera images over different range and turbidity condition, spanning $0\ cz$ to $16\ cz$. 100 frames are captured at each range and turbidity condition. We took the measurements in a lidar test tank and we increase the turbidity using Equate® liquid antacid, which is the standard method for mimicking the scattering of sea water. The liquid antacid has an albedo of 0.9[42], [43], where scattering albedo is defined as the ratio of scattering coefficient, b, to extinction coefficient, c. A C-Star transmissometer (Seabird Scientific) measures the turbidity throughout the experiments. We collect images with and without the submerged objects in order to independently measure the total amplitude and the backscatter amplitude.

B. Phasor Subtraction

Figure 3 shows a diagram of the phasor subtraction method, *i.e.* a visual representation of Eq. 2. Backscatter is plotted as a yellow phasor, the total amplitude and phase are plotted in green, and the object amplitude and phase are plotted in

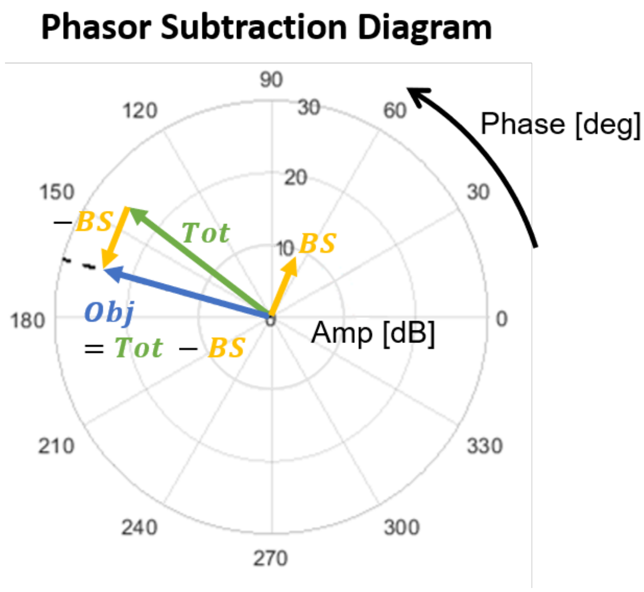

Fig. 3. An example of the phasor subtraction method. The total phasor is plotted in green, the backscatter phasor is plotted in yellow, and the object phasor is plotted in blue. The total phasor minus the backscatter phasor is also shown as the 180^o rotated backscatter phasor placed at the tip of the total phasor. This subtraction yields the object vector.

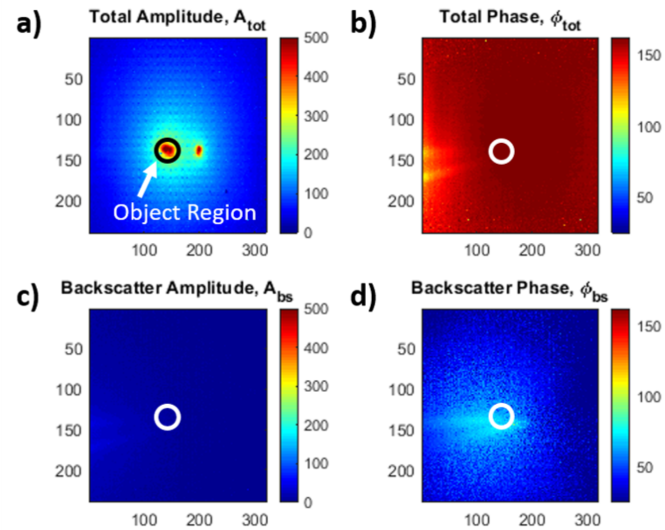

Fig. 4. Amplitude and phase images taken at 2.68 cz. a) Total amplitude: the laser spots are seen clearly, and the object region (the most accurate, high-intensity region) is circled b) Total phase: The phase is nearly uniform at 160^o. The backscatter can be seen on the left side of the image and appears at a closer phase than the object. Note that this is not the true phase value of the backscatter. The object contribution dominates the backscatter contribution so the measured phase of the backscatter is shifted towards the object. c) Backscatter amplitude: For these relatively clear conditions, the backscatter amplitude is very low and can be faintly seen on the left side of the image d) Backscatter phase: In phase, the backscatter can be more clearly seen propagating across the image from left to right. As it propagates the phase increases as the beam further from the ToF camera. Note that the backscatter phase is much lower compared to (b) because there is no object contributing to the measurement.

blue. Equation 2 is shown by placing the tail of the negative backscatter phasor at the tip of the total phasor. The resultant phasor (from the origin to the tip of the negative backscatter phasor) is the object phasor.

We show an example of the amplitude and phase images in Fig. 4 taken at 2.68 cz. For this relatively clear condition, the total phasor is dominated by the object and the collimated beam spots can be clearly seen in Fig. 4a, the total amplitude. Because we are using collimated beams rather than a diverging beam, we determine a region of interest (referred to as the Object Region) at the full-width, half-maximum of the larger beam spot. The object region is determined for each range in clear water and is used for each subsequent turbidity at that range. The object region is the region of maximum intensity and thus contains the most accurate phase information. The total phase is shown in Fig. 4b. While the image is dominated by the object (seen as a uniform phase distribution at 160^o), the backscatter can be seen as a region of lower phase on the left side of the image. Figure 4c shows the backscatter amplitude, which is low for this attenuation length, and Fig. 4d shows the backscatter phase. The backscatter phase can be seen on the left side of the image and the phase increases (gets further away) as the beam travels across the image from left to right. Note that the effect of the inherent ToF camera phasor summation can be seen by comparing the two phase measurements: Fig. 4b and Fig. 4d. In the backscatter phase image, the phase values of the beams as they enter the left side of the image are close to zero. However, in the total image, those same phase values are around 130^o. The phase values of the backscatter in the total phase image are inaccurate due to the strong influence of the object return at 160^o.

Figure 5 shows an example of the total phasor image and backscatter phasor image at 7.68 cz. At this higher attenuation length, the scene is dominated by backscatter. Figure 5a shows the total amplitude. Instead of seeing distinct beam spots, the total amplitude image shows a low intensity haze from the backscatter entering the scene from the left. The total backscatter, Fig. 5b, shows a phase gradient between the left and right side of the image, but the phase values are all very low due to the strong backscatter. Figure 5c shows that the backscatter amplitude is nearly identical to the total amplitude. The backscatter phase, Fig. 5d is similar to total phase. However, there is a clear difference in phase value on the right side of the two phase images, indicating the presence of an object in the scene.

Comparing Fig. 4 and Fig. 5 shows clearly the challenges imposed by backscattered light. In amplitude, the backscattered light completely masks the weaker signal from the object. In phase, we can recognize the presence of an object, but the measured phase value is inaccurate. Instead of 160^o, as expected and measured in Fig. 4b, the phase value is measured as 17^o, leading to a range measurement for the object which is much closer to the camera than the true distance to the object.

Figure 6 shows the object amplitude and phase at both 2.68 cz and 7.68 cz. These are the resultant images after the

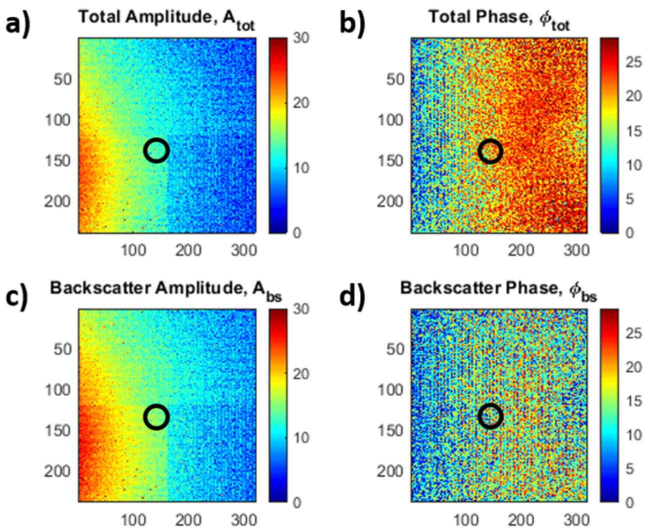

Fig. 5. Amplitude and phase images taken at 7.68 cz. a) Total amplitude: For this turbidity level, the object is dominated by the backscatter. The object region is circled b) Total phase: There is a clear change in phase between the left side of the image (backscatter) and right side of the image (object). However, the object phase is inaccurate because of the dominant backscatter contribution c) Backscatter amplitude: For these relatively turbid conditions, the backscatter amplitude is very similar to the total amplitude d) Backscatter phase: The backscatter phase still tends to increase as light propagates from the left side of the image to the right side of the image. Note the contrast to (b). While it is not clear from the amplitude data that an object is present, the difference in the phase values indicates the presence of a submerged object.

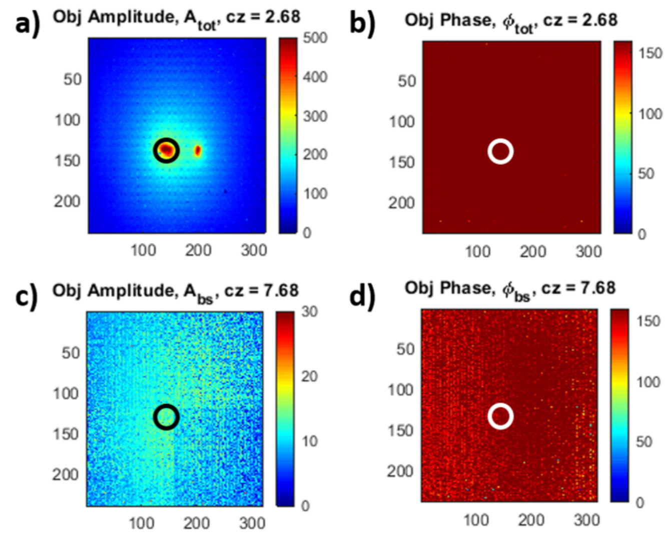

Fig. 6. Object amplitude and phase images for 2.68 cz and 7.68 cz after phasor subtraction of the backscatter. a) Object amplitude at 2.68 cz: compared to Fig. 4a the object amplitude is very similar to the total amplitude due to low turbidity. b) Object phase at 2.68 cz: compared to Fig. 4b the phase is even more uniform and the contribution of the backscatter on the left side of the image is no longer present. c) Object intensity at 7.68 cz: For these more turbid conditions, the object amplitude is very low due to attenuation. Compared to Fig. 5a there is no strong backscatter contribution. d) Object phase at 7.68 cz: Compared to Fig. 5b backscatter phasor subtraction yields an object phase much closer to the true phase value.

phasor subtraction (using Eq. 2) of the backscatter from the total images seen in Fig. 4 and Fig. 5. Figure 6a shows the object amplitude for 2.68 cz. Because the object was already dominant, it looks very similar to the total amplitude. Figure 6b shows the very uniform object phase at 160^o. Compared to the total phase, no backscatter contribution is present. The object amplitude for 7.68 cz is shown in Fig. 6c. The object amplitude is lower than the total amplitude, and there is no presence of backscatter on the left side of the image. The object phase for 7.68 cz is shown in Fig. 6d. The object phase is much closer to the expected value than the total phase, demonstrating that phasor subtraction is able to mitigate the impact of backscatter on the ToF measurements.

IV. Results

Figure 7 shows eight measurements on phasor diagrams. Amplitude is plotted on the r-axis in dB, and phase is plotted on the θ-axis in degrees. Each point corresponds to a pixel in the object region. The true phase of the submerged object is plotted as a dashed line at 160^o and 0^o corresponds to a range of $z = 0$. In Fig. 7a the total (object + backscatter) phasors are plotted. For low attenuation lengths, for example 2.68 cz the measured total phase falls at the expected phase, indicating the image is object dominated. As turbidity increases, the measured phase approaches 0^o as the backscatter comes to dominate. Figure 7b shows the backscatter phasors. As expected, as the turbidity increases the backscatter appears closer to the camera. Comparing the total and backscatter phasors we see that as the amplitude of the total phasor approaches the amplitude of the backscatter phasor, the total phase (*i.e* the phase measured by the camera) approaches the backscatter phase. Again, this shows the challenge posed by the underwater environment. Absorption leads to a rapid decrease in amplitude while backscatter adds a clutter signal which degrades the accuracy of phase measurement, leading to range measurements which are inaccurately read as much closer than the true object range. However, Fig. 7c plots the object phasor, and demonstrates the capabilities of the phasor subtraction method to mitigate the effects of scattering. Measuring the backscatter phasor and subtracting it from the total phasor corrects the phase value to be the true object phase for all measurements shown except the measurement at 10 cz which is limited by signal to noise.

Figure 8 shows the absolute percent range error (the measured range divided by the true range multiplied by 100) over attenuation lengths for the measured object range, the measured total range, and the measured backscattered range. Each data point is the average percent range error for a 2 attenuation lengths bin. For example, the data point at 1 cz is the mean percent error for all of the measurements which fall between 0 cz and 2 cz. The error bars are the upper and lower quartiles of the percent range errors. The results show three distinct regions: low turbidity, moderate turbidity, and high turbidity. In Region 1 (low turbidity: < 4 cz), the total range is accurate and not influenced much by backscatter. This is a result of the object phasor having a much greater

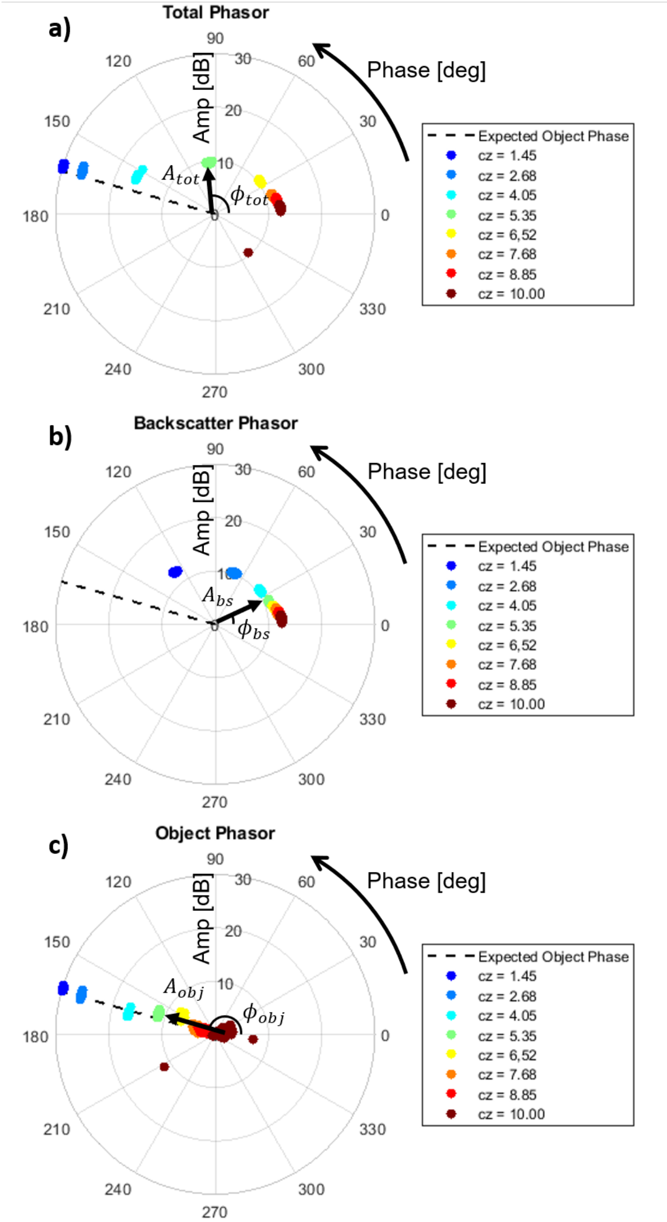

Fig. 7. ToF camera experimental results with an example vector for $cz = 5.35$. a) Total Phasor: For low values of cz, the measured phase is close to the expected phase value, 160^o. However, as the attenuation lengths increase and backscatter comes to dominate, the intensity decreases and the measured phase decreases, leading to range measurements which are much closer than the true range. b) Backscatter results: We see the expected result for backscatter. As attenuation lengths increase, the backscatter appears closer and closer to the camera. c) Object Phasor: after subtracting the backscatter phasor from the total phasor, the measured phase value is very close to the expected phase value for each attenuation length shown, excepting 10 cz.

magnitude than the backscatter phasor. Backscatter results are low amplitude and at a closer range than the object. In Region 3 (high turbidity > 10 cz), the backscatter vector dominates, The object vector is at or below the noise floor, and the total phasor calculates the range to the volumetric backscatter. Because the object return is absorption limited, phasor subtraction yields inaccurate results. In Region 2,

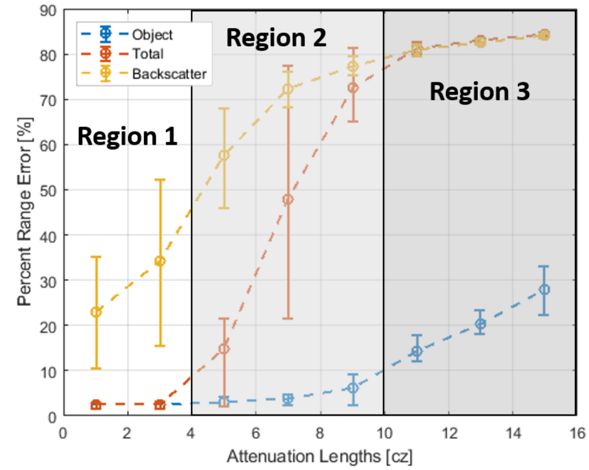

Fig. 8. Absolute percent range error vs. attenuation lengths is plotted for the total range, the object range, and the backscatter range. Each data point is the mean percentage range error over 2 attenuation lengths (for example, the data point at 1 cz is the mean percentage error of all the data that falls between 0 cz and 2 cz). The error bars show the lower and upper quartiles. The backscatter range error behaves as expected. As turbidity increases, the centroid of the backscatter range drifts closer to the camera. The total range error is less than 5% to 4 cz (*i.e.* without any processing the object is dominant and the ToF camera is accurate to 4 cz). After 4 cz the percent error increases before settling at the backscatter range, indicating that the backscatter is now dominate. By contrast, after background phasor subtraction the object percent range error is less than 5% until 8 cz. After $8cz$, low signal leads to noise-dominated, inaccurate measurement.

(moderate turbidity, $4 - 10$ cz) the magnitude of the object vector and backscatter vectors are commensurate. The total range (the range measured directly by the ToF camera) is not an accurate measure of either the object range or backscatter range. The vector subtraction approach is most effective in this region.

V. Conclusion

ToF cameras are investigated for use in underwater ranging and imaging. In turbid underwater environments, we show that accurate range performance for ToF cameras breaks down at 4.0 cz due to contribution of the backscatter. This work demonstrates that backscatter phasor subtraction doubles the operating range, achieving accurate range measurements at 8.0 cz. Future work will investigate higher power laser transmitters, as well as switching from collimated beams (which maximize the operating range of the ToF camera) to diverging beams (which maximize the area of the sensor which measures accurate information).

Acknowledgment

The work is funded by the Office of Naval Research on grant N00014-18-1-2291.

References

[1] G. Kattawar. “Time of flight lidar measurements as an ocean probe”. In: *Applied Optics* 11.2 (1972), pp. 662–666.

[2] G. C. Guenther. *Airborne Laser Hydrography*. Tech. rep. U.S. Department of Commerce, National Oceanic, Atmospheric Administration, National Ocean Service, Charting, and Geodetic Services, 1985.

[3] J. Jaffe. “Underwater Optical Imaging: The Past, the Present, and the Prospects”. In: *IEEE Journal of Oceanic Engineering* 40.3 (2015), pp. 683–700.

[4] F. R. Dalgleish, F. M. Caimi, W. B. Britton, et al. “Improved LLS imaging performance in scattering-dominant waters”. In: *Ocean Monitoring and Sensing* 7317 (2009), 73170E.

[5] C.D. Mobley. *Light and Water*. San Diego, CA: Elsevier Science, 1994.

[6] R. Smith and K. Baker. “Optical properties of the clearest natural waters”. In: *Applied Optics* 20.2 (1981), pp. 177–184.

[7] Fraser R. Dalgleish, Anni K. Vuorenkoski, and Bing Ouyang. “Extended-Range Undersea Laser Imaging: Current Research Status and a Glimpse at Future Technologies”. In: *Marine Technology Society Journal* 47.5 (2013), pp. 128–147.

[8] G.R. Fournier, D. Bonnier, J.L. Forand, et al. “Range-gated underwater laser imaging system”. In: *Optical Engineering* 32.9 (1993), pp. 2185–2190.

[9] E. A. McLean, H. R. Burris, and M. P. Strand. “Short-pulse range-gated optical imaging in turbid water”. In: *Applied Optics* 34.21 (1995), pp. 4343–4351.

[10] L. Mullen and V. Contarino. “Hybrid LIDAR-radar: Seeing through the scatter”. In: *IEEE Microwave Magazine* 1.3 (2000), pp. 41–48.

[11] F. Pellen, X. Intes, P. Olivard, et al. “Determination of sea-water cut-off frequency by backscattering transfer function measurement”. In: *Journal of Physics D: Applied Physics* 33.4 (2000), pp. 349–354.

[12] David W Illig, William D Jemison, and Linda J Mullen. “Independent component analysis for enhancement of an FMCW optical ranging technique in turbid waters”. In: *Applied Optics* 55.31 (2016), pp. C25–C33.

[13] Robert Lee, Alan Laux, and Linda Mullen. “Hybrid technique for enhanced optical ranging in turbid water environments”. In: *Optical Engineering* 53.5 (2014), 9 pp.

[14] B. Cochenour, S. O’Connor, and L. Mullen. “Suppression of forward-scattered light using high-frequency intensity modulation”. In: *Opt. Eng.* 53.5 (2014), p. 051406.

[15] J. K. Nash, R. W. Lee, and L. J. Mullen. “Tailoring of RF coded optical pulses for underwater 3D imaging”. In: *OCEANS 2015 - MTS/IEEE Washington, Washington, DC*. 2015, pp. 1–8.

[16] David W. Illig, Robert Lee, and Linda Mullen. “Statistical signal processing technique to reduce effects of forward scatter on underwater modulated pulse lidar”. In: *Ocean Sensing and Monitoring IX*. 2017.

[17] A.G. Luchinin and L.S. Dolin. “On dispersive properties of the photon-density waves in an anisotropic scattering medium”. In: *Radiophysics and Quantum Electronics* 59.2 (2016), pp. 145–152.

[18] Linda Mullen, Robert Lee, and David W. Illig. “Optimizing the performance of modulated pulse laser systems for imaging and ranging applications”. In: *Ocean Sensing and Monitoring IX*. 2017.

[19] Jian Wang, Jeng-Yuan Yang, Irfan M. Fazal, et al. “Terabit free-space data transmission employing orbital angular momentum multiplexing”. In: *Nature Photonics* 6 (2012), pp. 488–496.

[20] K. Morgan, Y. Li, W. Li, et al. “Multilevel quadrature amplitude multiplexing using coherently coupled orbital angular momentum modes”. In: *Optics Express* 26.9 (2016), pp. 12180–12190.

[21] D. Palacios, D. Rozas, and G. A. Swartzlander. “Observed Scattering into a Dark Optical Vortex Core”. In: *Physical Review Letters* 88.10 (2002), pp. 103902–103904.

[22] B. Cochenour, L. Rodgers, A. Laux, et al. “The detection of objects in a turbid underwater medium using orbital angular momentum (OAM)”. In: *Ocean Sensing and Monitoring IX*. Vol. 10186. International Society for Optics and Photonics. 2017, p. 1018603.

[23] Austin Jantzi, William Jemison, Alan Laux, et al. “Enhanced underwater ranging using an optical vortex”. In: *Optics Express* 26.3 (2018), pp. 2668–2674.

[24] Austin Jantzi, Luke Rumbaugh, and William Jemison. “Spatial coherence filtering for scatter rejection in underwater laser systems”. In: *Ocean Sensing and Monitoring XI*. Vol. 11014. International Society for Optics and Photonics. 2019, p. 1101406.

[25] K.S. Morgan, E.G. Johnson, and B.M. Cochenour. “Attenuation of beams with orbital angular momentum for underwater communication systems”. In: *OCEANS 2015 - MTS/IEEE Washington, Washington, DC*. 2015, pp. 1–3.

[26] Joshua Baghdady, Keith Miller, Kaitlyn Morgan, et al. “Multi-gigabit/s underwater optical communication link using orbital angular momentum multiplexing”. In: *Optics express* 24.9 (2016), pp. 9794–9805.

[27] B. Cochenour, K. Morgan, K. Miller, et al. “Propagation of modulated optical beams carrying orbital angular momentum in turbid water”. In: *Applied Optics* 55.31 (2016), pp. C34–C38.

[28] T. Doster and A.T. Watnik. “Machine learning approach to OAM beam demultiplexing via convolutional neural networks”. In: *Applied Optics* 56.12 (2017), pp. 3386–3396.

[29] A.E. Willner, Z. Zhao, Y. Ren, et al. “Underwater optical communications using orbital angular momentum-based spatial division multiplexing”. In: *Optics Communications* 408 (2018), pp. 21–25.

[30] K. Morgan, Y. Li, W. Li, et al. “Higher Order Bessel Beams Integrated in Time (HOBBIT) for Underwater Sensing and Metrology”. In: *Conference on Lasers and Electro-Optics (CLEO)*. 2019.

[31] H. Song, H. Song, R. Zhang, et al. “Experimental Mitigation of Atmospheric Turbulence Effect Using Pre-Signal Combining for Uni- and Bi-Directional Free-Space Optical Links with Two 100-Gbit/s OAM-Multiplexed Channels”. In: *Journal of Lightwave Technology* 38.1 (2020), pp. 82–89.

[32] P.L. Neary, A.T. Watnik, K.P. Judd, et al. “Machine learning-based signal degradation models for attenuated underwater optical communication OAM beams”. In: *Optics Communications* 474 (2020), p. 126058.

[33] S. Avramov-Zamurovic, A.T. Watnik, J.R. Lindle, et al. “Machine learning-aided classification of beams carrying orbital angular momentum in highly turbid water”. In: *Journal of the Optical Society of America A* 37.10 (2020), pp. 1662–1672.

[34] A. Jantzi, W. Jemison, D. Illig, et al. “Axicons for improved lidar performance”. In: *Ocean Sensing and Monitoring XII*. 2020.

[35] Austin Jantzi, William Jemison, David Illig, et al. “Spatial and temporal domain filtering for underwater lidar”. In: *JOSA A* 38.10 (2021), B10–B18.

[36] Stefan May, David Dröschel, Stefan Fuchs, et al. “Robust 3D-mapping with time-of-flight cameras”. In: *2009 IEEE/RSJ International Conference on Intelligent Robots and Systems*. IEEE. 2009, pp. 1673–1678.

[37] Kevin V Mack, Prashant Athavale, William D Jemison, et al. “Restoration of time-of-flight (ToF) underwater images using TV regularization”. In: *Ocean Sensing and Monitoring XIII*. Vol. 11752. International Society for Optics and Photonics. 2021, 117520N.

[38] Luke K Rumbaugh, John Will, Joshua R Thomson, et al. “Experiments using a 525 nm time-of-flight camera for object imagining and ranging in clear and turbid water”. In: *Ocean Sensing and Monitoring XIV*. Vol. 12118. SPIE. 2022, pp. 120–131.

[39] Texas Instruments. “Time-of-Flight Camera—An Introduction”. In: *Technical White Paper, Literature No. SLOA190B* 10 (2014).

[40] Nikhil Naik, Achuta Kadambi, Christoph Rhemann, et al. “A light transport model for mitigating multipath interference in time-of-flight sensors”. In: *Proceedings of the IEEE Conference on Computer Vision and Pattern Recognition*. 2015, pp. 73–81.

[41] Keita Yamazaki. “Analysis of Phasor Distortions by Fog in Time-of-Flight Measurement”. In: (2020).

[42] Alan Laux, R. Billmers, Linda Mullen, et al. “The a,b,c’s of oceanographic lidar predictions: a significant step towards closing the loop between theory and experiment”. In: *Journal of Modern Optics* 49.3/4 (2002), pp. 439–451.

[43] Linda Mullen, Derek Alley, and Brandon Cochenour. “Investigation of the effect of scattering agent and scattering albedo on modulated light propagation in water”. In: *Applied Optics* 50.10 (2011), pp. 1396–1404.